CrossMark

ORIGINAL PAPER

J. Ravnik · C. Marchioli · A. Soldati

Application limits of Jeffery's theory for elongated particle torques in turbulence: a DNS assessment

This paper is dedicated to the memory of Franz Ziegler

Abstract Non-spherical particles suspended in fluid flows are subject to hydrodynamic torques generated by fluid velocity gradients. For small axisymmetric particles, the most popular formulation of hydrodynamic torques is that given by Jeffery (Proc R Soc Lond A 102:161–179, 1922), which is valid for uniform shear flow in the viscous Stokes regime. In the lack of simple alternative formulations outside the Stokes regime, the Jeffery formulation has been widely applied to inertial particles in turbulent flows, where it is bound to produce inaccurate results. In this paper we quantify the statistical error incurred when the Jeffery formulation is used to study the motion of elongated axisymmetric particles under nonlinear shear flow conditions. Considering the archetypical case of prolate ellipsoidal particles in turbulent channel flow, we show that error for ellipsoids of the same length, l, as the Kolmogorov scale of the flow, η_K, is indeed small (order 1%) but increases exponentially up to $l \simeq 10\eta_K$ before becoming almost independent of elongation.

1 Introduction

Suspensions of non-spherical particles in turbulent flow are commonly found in a broad variety of industrial applications (e.g., pulp and paper making, colloids and polymer manufacturing, post-combustion soot emissions) and environmental processes (e.g., atmospheric pollen dispersion, plankton and marine snow dynamics in water bodies, ice cloud formation). These suspensions are characterized by complex particles–fluid interactions that depend strongly on particle shape and orientation. In recent years, a growing number of numerical [7,9–11,14,21,28,35,46–48] and experimental studies [8,15,17,26,31,33,36,42] have investigated such interactions, considering in particular the case of spheroidal particles translating and rotating at low concentrations in a turbulent flow (see [43] for a review). Limiting our discussion to numerical studies, analyses have relied on approaches that are routinely adopted to simulate turbulent dispersed flows [2]. The most detailed approach is the particle-resolved approach, which solves for the flow around each particle prescribing exact boundary conditions for forces and torques at the particle surface. Computational costs associated with the calculation of these boundary conditions, however, restrict current application of this approach to relatively small

J. Ravnik
Faculty of Mechanical Engineering, University of Maribor, Smetanova 17, 2000 Maribor, Slovenia
E-mail: jure.ravnik@um.si

C. Marchioli (✉) · A. Soldati
Department of Engineering and Architecture, University of Udine, Via delle Scienze 206, 33100 Udine, Italy
E-mail: cristian.marchioli@uniud.it

A. Soldati
Institute of Fluid Mechanics and Heat Transfer, TU Wien, Getreidemarkt 9, 1060 Wien, Austria
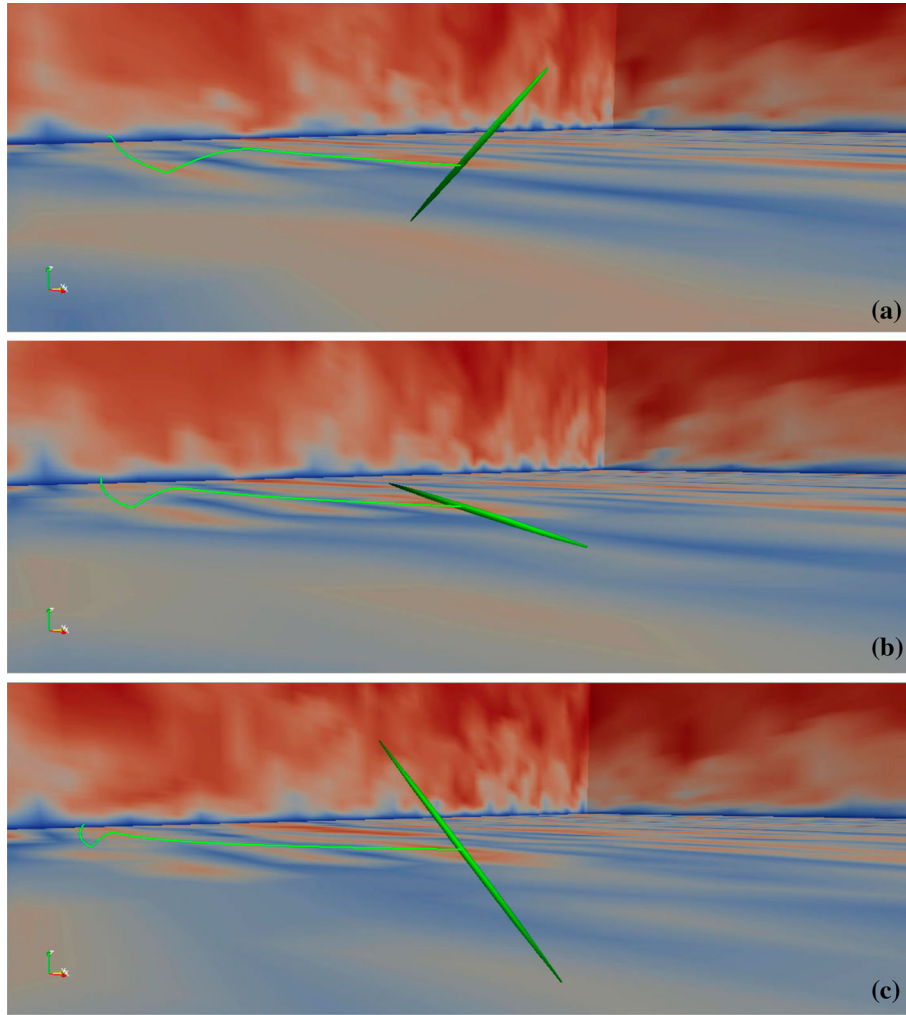E-mail: alfredo.soldati@tuwien.ac.at

Fig. 1 Snapshots of one rigid fiber translating and rotating in turbulent channel flow (simulation parameters: shear Reynolds number $Re_\tau = 150$; fiber Stokes number $St = 25$; fiber aspect ratio $\lambda = 50$—See Sect. 2 for definitions). Colors from blue to red in the background represent increasingly high values of the streamwise fluid velocity. The green solid line shows the trajectory of the center of mass of the fiber. The time lag between each panel is 3 in wall units (color figure online)

numbers of particles [19]. Hence, the most applied approach to simulate large swarms of particles is the point-particle approach, in which particles are tracked individually, determining their translational dynamics by Newton's second law and their rotational dynamics by conservation of angular momentum for a rigid body. This Lagrangian approach is valid in the limit of particle size much smaller than the Kolmogorov length scale and has been widely used to investigate the motion of small spheroidal particles in simple shear flows [11,16,39] as well as turbulent flow [14,20–22,24,25,44,48]. One qualitative example of application is provided in Fig. 1, where the motion of a prolate spheroid (mimicking a rigid fiber) in the near-wall region of a turbulent channel flow is shown. The actual length of the fiber is magnified to highlight its rotational motion, mostly characterized by tumbling in the mean-flow-gradient plane. Such motion results from the application of a lumped-parameter model that is valid in the limit of dilute flow conditions (one-way coupling). Albeit simplified, the model incorporates the dependence of the hydrodynamic viscous drag force on the particle orientation, which is known to create crucial differences between elongated fibers and equivalent spherical particles. This has proven sufficient to capture the key physics coupling particle orientation to the velocity gradients and coupling particle translational motion to particle rotation (see [43] for a detailed review). The large majority of numerical studies is based on such a model, which computes the hydrodynamic resistance forces (drag, in particular) and torques acting on the particles using expressions derived for creeping flow conditions [4,5,13,18]: Under these conditions, the trajectory of individual particles can be calculated using only the

flow velocities and velocity gradients at the position of the particle's center of mass. The first formulation was proposed by [18] for the case of a single inertia-free ellipsoid in uniform shear flow under Stokes conditions. This formulation was later revisited by Bretherthon [6], who added the aspect ratio of the ellipsoid as shape parameter to incorporate the effect of particle elongation. Further theoretical work has led to extensions of the Jeffery equations for forces and torques to arbitrary flow fields (e.g., [4,5]) and to non-axisymmetric ellipsoids (e.g., [16]).

An important assumption, inherent in these formulations, is that the Reynolds number of the particle, Re_p, is very small (ideally equal to zero): Away from this limit, inaccurate estimations of forces and torques should be expected. In most real-life situations, however, particles are characterized by a finite value of Re_p [2,43,46] because the particle inertia is high enough to generate a non-negligible particle-to-fluid velocity difference and/or at least one particle dimension is large relative to the Kolmogorov scale. In this latter case, changes in the fluid velocity gradients along the particle may occur due to nonlinear variations of the velocity profile. Such restrictions seem to pose strong limits to the applicability of the Jeffery equations to situations of practical interest, particularly for the calculation of hydrodynamic torques in turbulent flow conditions: The sensitivity of rotational dynamics to errors associated with the velocity gradients is significantly higher than the sensitivity of translation dynamics to errors associated with the velocity [22,46]. Nevertheless, these equations have been verified experimentally [1,11,27,30,31,40,41], even for particles longer than the Kolmogorov scale [29]. They have also been employed in many studies to investigate the behavior of anisotropic particles in laminar and turbulent flows [7,9,14,21,22,30,38,48], even outside the small-Re_p limit (see [21]; Zhao et al. [9]; Zhao et al. [22] among others). In this context, an important open issue is the level of inaccuracy associated with the use of the Jeffery formulation to calculate the hydrodynamic torques at small, yet finite Re_p. Up to now, no quantification of such inaccuracy has been provided and a clear assessment of the application limits of the Jeffery formulation is missing. In this paper, we provide this assessment for the reference case of elongated prolate ellipsoids (mimicking a suspension of rigid fibers) in fully developed turbulent channel flow. Particles with different inertia (Stokes numbers from 1 to 25) and size (length l ranging from 0.1 to 36 time the Kolmogorov length scale η_K) are considered. The analysis is based on statistics of the error incurred when the Jeffery torques are used in the angular conservation momentum equations under nonlinear shear flow conditions, exploiting a direct numerical simulation database. Our objective is to determine an upper bound for the ratio l/η_K above which the error becomes too high to be tolerated.

2 Governing equations

The carrier fluid is Newtonian (with dynamic viscosity μ and kinematic viscosity ν) and incompressible (with density ρ). The fluid motion is governed by the following dimensionless mass and momentum conservation equations, in vector form:

$$\nabla \cdot \mathbf{u} = 0; \qquad \frac{\partial \mathbf{u}}{\partial t} + (\mathbf{u} \cdot \nabla)\mathbf{u} = -\nabla p + \frac{1}{Re_\tau}\nabla^2 \mathbf{u}, \tag{1}$$

where $\mathbf{u}$ and p denote the fluid velocity and the pressure, respectively. The frictional Reynolds number is $Re_\tau = hu_\tau/\nu$, with h the channel half-height, the wall-friction velocity $u_\tau = \sqrt{\tau_{\text{wall}}/\rho}$ is the wall-friction velocity based on the wall shear stress τ_{wall}. The flow is driven by a constant mean pressure gradient and is unaffected by the presence of the fibers (one-way coupling).

Particles are modeled as pointwise rigid prolate spheroids with semi-major axis b, semi-minor axis a and aspect ratio $\lambda = b/a$. Particle translation and rotation are governed by the following equations:

$$m_p \frac{d\mathbf{u}_p}{dt} = \mathbf{F}_D, \tag{2}$$

$$\frac{d(\mathbf{I} \cdot \boldsymbol{\omega}')}{dt} + \boldsymbol{\omega}' \times (\mathbf{I} \cdot \boldsymbol{\omega}') = \mathbf{M}', \tag{3}$$

where ρ_p is particle density, and $m_p = 4\pi a^3 \lambda \rho_p/3$ is particle mass. In Eq. (2), $\mathbf{u}_p = d\mathbf{x}_p/dt$ is the translational particle velocity and $\mathbf{F}_D$ is the drag force acting on the particle, both formulated in the *inertial* frame of reference $\mathbf{x} = \langle x, y, z \rangle$ with x, y and z the streamwise, spanwise and wall-normal flow directions, respectively. In Eq. (3), $\mathbf{I}$ is the moment of inertia tensor, $\boldsymbol{\omega}'$ is the angular velocity of the particle and $\mathbf{M}'$ is the torque. Both $\boldsymbol{\omega}'$ and $\mathbf{M}'$ are formulated in the *particle* frame of reference $\mathbf{x}' = \langle x', y', z' \rangle$ with origin at the fiber center of mass and

coordinate axes x', y' and z' aligned with the principal directions of inertia. In the limit of pointwise particles, the surrounding flow can be considered as Stokesian and the drag force $\mathbf{F}_D$ can be expressed as [4,5]:

$$\mathbf{F}_D = \mu \mathbf{R} \mathbf{K}' \mathbf{R}^{\mathrm{T}} \cdot (\mathbf{u}_f - \mathbf{u}_p) = \mu \mathbf{K} \cdot \Delta \mathbf{u}, \tag{4}$$

where $\mathbf{R}$ is the orthogonal transformation matrix which relates the same vector in the two above-mentioned frames through the linear transformation $\mathbf{x} = \mathbf{R} \mathbf{x}'$ ($\mathbf{R}^{\mathrm{T}}$ being its transpose), $\mathbf{u}_f$ is the fluid velocity at the fiber position, $\mathbf{K}'$ is the resistance tensor in the particle frame [13,44], and $\Delta \mathbf{u} = \mathbf{u}_f - \mathbf{u}_p$ is the relative velocity between the fluid and the particle at the center of mass of the particle (referred to as slip velocity hereinafter). Equation (4) is valid for a particle with arbitrary shape under creeping flow conditions, namely small fiber Reynolds number, $Re_p = 2a \mid \Delta \mathbf{u} \mid /\nu$.

The Jeffery torques divided by the moment of inertia of the ellipsoid are given as [18]

$$\begin{Bmatrix} M_J^x/I_{x'} \\ M_J^y/I_{y'} \\ M_J^z/I_{z'} \end{Bmatrix} = \frac{20}{(a^+)^2} \frac{\rho_f}{\rho_p} \begin{Bmatrix} \frac{1}{(\beta_0 + \lambda^2 \gamma_0)} \left[\frac{1-\lambda^2}{1+\lambda^2} f' + (\xi' - \omega_{x'}) \right] \\ \frac{1}{(\alpha_0 + \lambda^2 \gamma_0)} \left[\frac{\lambda^2 - 1}{1+\lambda^2} g' + (\eta' - \omega_{y'}) \right] \\ \frac{1}{(\alpha_0 + \beta_0)} (\chi' - \omega_{z'}) \end{Bmatrix}, \tag{5}$$

where ρ_f is the fluid density, f', g' are elements of the deformation rate tensor, and ξ', η' and χ' are elements of the spin tensor:

$$f' = \frac{1}{2} \left(\frac{\partial u_{z'}}{\partial y'} + \frac{\partial u_{y'}}{\partial z'} \right), \qquad g' = \frac{1}{2} \left(\frac{\partial u_{x'}}{\partial z'} + \frac{\partial u_{z'}}{\partial x'} \right), \tag{6}$$

$$\xi' = \frac{1}{2} \left(\frac{\partial u_{z'}}{\partial y'} - \frac{\partial u_{y'}}{\partial z'} \right), \quad \eta' = \frac{1}{2} \left(\frac{\partial u_{x'}}{\partial z'} - \frac{\partial u_{z'}}{\partial x'} \right), \quad \chi' = \frac{1}{2} \left(\frac{\partial u_{y'}}{\partial x'} - \frac{\partial u_{x'}}{\partial y'} \right). \tag{7}$$

The non-dimensional coefficients α_0, β_0 and γ_0 are given as [13]:

$$\alpha_0 = \beta_0 = \frac{\lambda^2}{\lambda^2 - 1} + \frac{\lambda}{2(\lambda^2 - 1)^{3/2}} \ln \frac{\lambda - \sqrt{\lambda^2 - 1}}{\lambda + \sqrt{\lambda^2 - 1}}, \tag{8}$$

$$\lambda^2 \gamma_0 = -\frac{2\lambda^2}{\lambda^2 - 1} - \frac{\lambda^3}{(\lambda^2 - 1)^{3/2}} \ln \frac{\lambda - \sqrt{\lambda^2 - 1}}{\lambda + \sqrt{\lambda^2 - 1}}. \tag{9}$$

Equation (2) can be recast as

$$\frac{d\mathbf{u}_p}{dt} = \frac{\mathbf{K} \cdot (\mathbf{u}_f - \mathbf{u}_p)}{St} f(\lambda), \tag{10}$$

where the particle Stokes number is defined as [37]:

$$St = \frac{4}{3} \frac{\rho_p}{\rho_f} (a^+)^2 \lambda f(\lambda), \qquad f(\lambda) = \frac{\ln(\lambda + \sqrt{\lambda^2 - 1})}{6\sqrt{\lambda^2 - 1}}, \tag{11}$$

where the superscript + indicates wall units, obtained using the friction velocity u_τ based on the mean wall shear stress and the fluid kinematic viscosity, ν ($a^+ = au_\tau/\nu$).

3 Simulation details

The statistics presented in this paper are relative to a turbulent Poiseuille channel flow of an incompressible Newtonian fluid at shear Reynolds number $Re_\tau = u_\tau h/\nu = 150$. Here, u_τ is the friction velocity based on the mean wall shear stress and on fluid density, ν is the fluid kinematic viscosity and h is the channel half-height. The corresponding bulk Reynolds number is $Re = u_0 h/\nu = 2250$, where $u_0 = 1.77 \, m/s$ is the bulk velocity. Direct numerical simulation of turbulence was performed using a pseudo-spectral flow solver [20,21]. Periodic boundary conditions were imposed in the streamwise (x) and spanwise (y) directions while no-slip boundary

Table 1 Summary of simulation parameters for the particles

a^+	λ	$\dfrac{l^+}{\eta_K^+}$	$\left.\dfrac{\rho_p}{\rho_f}\right|_{St=1}$	$\left.\dfrac{\rho_p}{\rho_f}\right|_{St=5}$	$\left.\dfrac{\rho_p}{\rho_f}\right|_{St=25}$
0.036	3	0.108	4276.19	–	–
0.12	3	0.36	34.72	173.61	868.06
0.36	3	1.08	42.76	213.81	1069.05
0.36	10	3.6	26.58	132.88	664.42
0.72	10	7.2	6.64	33.22	166.1
0.36	50	18	17.36	86.79	433.95
0.72	50	36	4.34	21.7	108.49

The smallest value of the Kolmogorov length scale in the channel, $\eta_K^+ = 2$, is used to normalize particle length $l^+ = 2a^+\lambda$. The shortest particles were not simulated at $St = 5$ and 25 because the corresponding density, yield by Eq. (11), would have been too high and not representative of any known material

conditions were imposed at the two walls. Time integration was performed using a second-order Adams–Bashforth scheme for the nonlinear terms, which are calculated upon de-aliasing in the periodic directions, and an implicit Crank–Nicolson scheme for the viscous terms. The domain size is $4\pi h \times 2\pi h \times 2h$ in the streamwise, spanwise and wall-normal directions, respectively. This domain is discretized by $128 \times 128 \times 129$ grid nodes.

Lagrangian tracking was performed considering particles with Stokes number $St = 1, 5, 25$ and aspect ratio $\lambda = 3, 10, 50$. The simulation parameters for each set of particles are summarized in Table 1. Note that, in the present flow configuration, the Kolmogorov scale ranges from a minimum value $\eta_{K,\min}^+ \simeq 2$ (in wall units) close to the wall to a maximum $\eta_{K,\max}^+ \simeq 4$ in the center of the channel [32]: In Table 1, the dimensionless particle length $l^+ = 2a^+\lambda$, in wall units, is normalized by $\eta_K^+ = \eta_{K,\min}^+$. The same assumption is made in the following section to provide conservative estimates of the application limits of the Jeffery formulation for torques. For each combination of values for St and λ (with the exception of $\lambda = 3$ and $St = 5, 25$, which would have yielded unphysically high values of the particle density), $N_p = 10^5$ particles were injected into the flow with random orientation and velocity equal to the fluid velocity at the particle release position. The particle motion equations were solved using a 4th order Runge–Kutta scheme with a time step $dt^+ = 0.1$ in wall units, equal to one-tenth of the smaller Stokes number considered. Such step size is small enough to ensure accurate time integration of the particle motion equations [12]. Periodic boundary conditions are imposed on particles in both streamwise and spanwise directions, whereas elastic reflection is applied when either of the particle's ends touches the wall. Elastic reflection was chosen since it is the most conservative assumption when studying the reasons of particle preferential concentration in a turbulent boundary layer. The numerical implementation is based on the work of Ravnik and Hribersek [34]. Particle statistics were computed starting at time $t^+ = 300$ upon particle injection: This time span is long enough to ensure that the initial conditions have no influence of the statistics. Statistics were then gathered for a time span $\Delta t^+ = 1000$.

4 Results

As mentioned in Introduction, the Jeffery formulation for torques is based on the assumption that the fluid velocity field varies linearly along the particle. In this case, the formulation is accurate and the velocity gradients at the particle center of mass can be used to compute the particle rotational dynamics [18]. In a turbulent flow, this condition is met when particles are smaller than the Kolmogorov scale. However, recent experimental results on the rotation rate of rigid rod-like particles in homogeneous isotropic turbulence [30,38] have shown that, compared to inertialess tracers, the particle rotation rate variance does not change up to particle lengths of about $7\eta_K$. This suggests that the Jeffery formulation might be applicable to particles as long as (or even longer than) the Kolmogorov eddies, with tolerable accuracy in the estimation of the torques. The objective of this section is precisely to quantify this accuracy and assess the application limits of Eq. (5): This is done by characterizing statistically the error associated with the use of the velocity gradients at the particle center of mass.
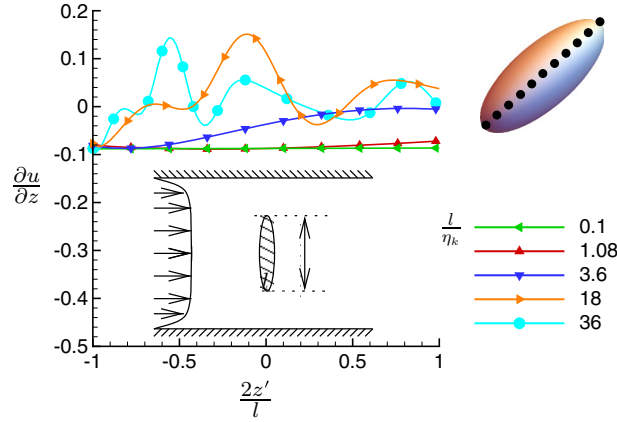
Fig. 2 Profiles of the instantaneous velocity gradient $\partial u/\partial z$ along the particle at varying particle length. The values of $\partial u/\partial z$ refer to the locations shown in the top-right inset. To emphasize the change in $\partial u/\partial z$ a particle oriented perpendicularly to the mean flow direction and located in the channel center is considered

4.1 Assessment of the linear-velocity assumption

We examine first the behavior of the flow field along the particle length l. To this aim, we sampled the fluid velocity gradients at eleven locations uniformly distributed along l for each particle in each set. These locations are indicated in the top-right inset of Fig. 2, which shows the behavior of one reference velocity gradient component, $\partial u/\partial z$: This specific component was chosen because it is associated with the main shear component in the flow. The profiles correspond to different values of l^+/η_K^+ and refer to a particle that is instantaneously oriented in the cross-sectional plane with respect to the mean flow direction: For this particular orientation, $\partial u/\partial z$ is expected to exhibit the largest spatial variation. As could be anticipated, the velocity gradient is indeed uniform for the short particles ($l^+/\eta_K^+ = 0.1$), meaning that the velocity field varies linearly and can thus be approximated using a Taylor series expansion around the particle center, as done by Jeffery to derive Eq. (5). However, the profile remains nearly flat also for $l^+/\eta_K^+ = 1.08$, and smooth variations are observed only starting from $l^+/\eta_K^+ = 3.6$. As the particle length increases further, changes in the velocity gradient become more and more evident, with rather large oscillations for $l^+/\eta_K^+ \geq 18$: For these particles, which are likely to span several small-scale turbulent structures at a time, the surrounding velocity flow field varies nonlinearly. We remark here that the behavior of the velocity gradients depends strongly on the orientation of the particle relative to the mean flow. When the particle is oriented in the streamwise direction, we observe much smaller variations for all gradient components (results not shown): In this situation, application of the Jeffery formulation beyond the Stokes regime may still provide accurate estimates of the hydrodynamics torques. The observation is particularly relevant for the case of inertial particles accumulating in the near-wall region of the channel, which are known to preferentially align in the mean flow direction, namely the direction of strongest Lagrangian stretching [45]. More so because orientation plays an important role particularly for short particles, while having weaker effects on longer particles: Short particles (e.g., sub-Kolmogorov) interact with a single small-scale flow structure at a time and the fluid velocity variation they "see" changes depending on their orientation; on the other hand, long particles (e.g., spanning a few Kolmogorov length scales) may be subject to the action of different flow structures and the variation of fluid velocities "seen" has weak statistical dependence on orientation.

To characterize the variation of the fluid velocities and velocity gradients along the particle, we consider two norms. The first norm is defined as

$$||\mathbf{u}_f^J - \mathbf{u}_f^F|| = \sqrt{\frac{\sum_{s=1}^{11}(\mathbf{u}_{f,s}^J - \mathbf{u}_{f,s}^F)^2}{\sum_{s=1}^{11}(\mathbf{u}_{f,s}^F)^2}}, \tag{12}$$

where

$$\mathbf{u}_f^J(\mathbf{r} + \Delta\mathbf{r}) = \mathbf{u}_f(\mathbf{r}) + \nabla\mathbf{u}_f \cdot \Delta\mathbf{r} \tag{13}$$

is the Taylor expansion of the fluid velocity around the (ellipsoidal) particle, truncated after the leading-order term as done by [18], and $\mathbf{u}_f^F$ is the exact fluid velocity obtained from the DNS database. On the right hand
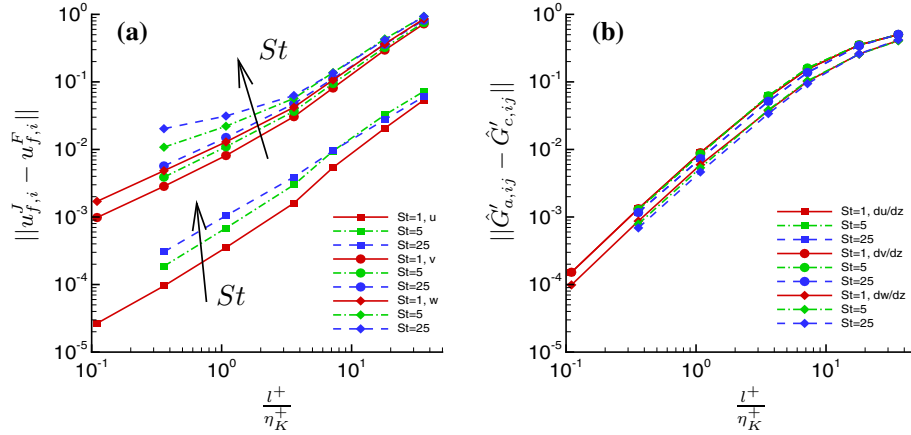
Fig. 3 Rms error (norm) for fluid velocities (**a**) and velocity gradients along the z'-axis in the particle frame (**b**) at varying particle length, normalized by the reference Kolmogorov length scale $\eta_k^+ = 2$

side of Eq. (12), $\mathbf{u}_f^J$ and $\mathbf{u}_f^F$ are averaged over the particle length using their discrete values at the uniformly distributed locations visualized in the top-right inset of Fig. 1, indicated by the subscript s in the summation. The second norm is defined as

$$||\hat{\mathbf{G}}_a' - \hat{\mathbf{G}}_c'|| = \frac{|\hat{\mathbf{G}}_a' - \hat{\mathbf{G}}_c'|}{\sqrt{2\left[(\hat{\mathbf{G}}_a')^2 + (\hat{\mathbf{G}}_c')^2\right]}}, \tag{14}$$

where $\hat{\mathbf{G}}_a'$ is the average value of the velocity gradient tensor along the particle (the averaging procedure is the same adopted for the velocity), and $\hat{\mathbf{G}}_c'$ is the velocity gradient tensor evaluated at the particle center of mass. Both gradients are computed in the particle frame (denoted by the superscript $'$); hence, the norm provides an estimate of the root-mean-square (rms) error associated with the use of Eq. (5) to solve for Eq. (5).

The behavior of these two norms is shown in Fig. 3, for the different velocity components ($||u_{f,i}^J - u_{f,i}^F||$, Fig. 3a) and for the velocity gradients along the z'-axis in the particle frame ($||\hat{G}_{a,iz}' - \hat{G}_{c,iz}'||$, Fig. 3b). As expected, a systematic increase of both $||u_{f,i}^J - u_{f,i}^F||$ and $||\hat{G}_{a,iz}' - \hat{G}_{c,iz}'||$ with particle length is observed. For the velocity norm (Fig. 3a), while following the same qualitative trend with l^+/η_K^+, the difference is smallest for the streamwise component and significantly larger for the spanwise and wall-normal components. This indicates that the error associated with the streamwise velocity is nearly negligible compared to the error associated with the spanwise and wall-normal velocities. Comparing particles with different inertia, we observe that short particles ($l^+/\eta_K^+ \leq 1$) with high inertia experience larger differences in velocity approximation than low-inertia particles. The norm of the wall-normal velocity gradients (Fig. 3b) reaches a value of about $5 \cdot 10^{-3}$ when the particle length equals the Kolmogorov length scale: This means that an error below 1% error is expected in particle tracking. Overall, all nine components of the gradient tensor yield values of the rms error with the same order of magnitude, the largest being observed for the wall-normal components. This finding is in qualitative agreement with the fact that the largest velocity variation occurs along the major axis of the particle when it is oriented perpendicular to the mean flow.

4.2 Assessment of the applicability limit of the Jeffery formulation for torques

To assess the applicability limit of Eq. (5) we consider again two different norms. The first norm is expressed as

$$||\mathbf{M}_J^a - \mathbf{M}_J^c|| = \frac{|\mathbf{M}_J^a - \mathbf{M}_J^c|}{\sqrt{2\left[(\mathbf{M}_J^a)^2 + (\mathbf{M}_J^c)^2\right]}}, \tag{15}$$
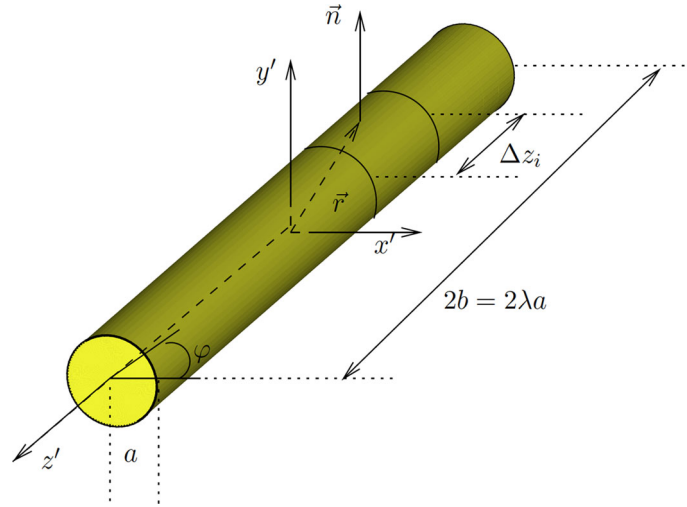
Fig. 4 Schematic of rod-like particle with cylindrical shape. To compute averaged quantities along the particle length, the particle surface is discretized into equally spaced sections of length Δz_i

where $\mathbf{M}_j^a$ is the torque calculated using the velocity gradients averaged along the particle length and $\mathbf{M}_j^c$ is the torque calculated using only the velocity gradients at the particle center of mass. In this case, the particle is modeled as a prolate ellipsoid.

The second norm is obtained extending the assessment to rod-like particles, modeled as cylinders of length $2b$ and cross-section diameter $2a$. For these particles, it is easy to compute the torque by discretizing the cylinder into equally sized sections along the major axis (from end to end), calculating for each section the contribution to the total torque associated with the velocity gradients at the section's center of mass. Let Δz_j be the length of the j-th section and let $\hat{\mathbf{G}}'_i$ be the velocity gradient measured at the center of mass of the j-th section (see Fig. 4). Then, the torque generated by the flow around the j-th section can be written as

$$\mathbf{M}_j = \mu \int_{\Gamma_j} \mathbf{r} \times \hat{\mathbf{G}}'_j \cdot \mathbf{n} d\Gamma, \tag{16}$$

where Γ_j is the area of the section, $\mathbf{r}$ is the location vector pointing from the cylinder's center to the surface of the section, and $\mathbf{n}$ is the unit vector normal to the cylinder surface. The fluid velocity gradient at the section's center is computed upon trilinear interpolation and is assumed constant over the lateral surface of the section: this way, integration of Eq. (16) is purely geometrical.

Taking into account the moments of inertia of a cylinder:

$$I_{z'} = \pi \lambda a^5 \rho_p, \qquad I_{x'} = I_{y'} = \pi \lambda a^5 \rho_p \frac{3 + 4\lambda^2}{6}, \tag{17}$$

the torques can be written as follows (in wall units):

$$\begin{pmatrix} M_i^x/I_{x'} \\ M_i^y/I_{y'} \\ M_i^z/I_{z'} \end{pmatrix} = \frac{1}{(a^+)^2} \frac{\rho_f}{\rho_p} \left[\begin{pmatrix} \frac{6}{3+4\lambda^2}(-f' + (\xi' - \omega_{x'})) \\ \frac{6}{3+4\lambda^2}(g' + (\eta' - \omega_{y'})) \\ 0 \end{pmatrix}_{z'=-b} + \right.$$
$$\left. + \sum_{i=1}^{n} \frac{\Delta z_i'^+}{\lambda a^+} \begin{pmatrix} \frac{6}{3+4\lambda^2}(f' + (\xi' - \omega_{x'})) \\ \frac{6}{3+4\lambda^2}(-g' + (\eta' - \omega_{y'})) \\ 2(\chi' - \omega_{z'}) \end{pmatrix}_{z'=z_i'} + \begin{pmatrix} \frac{6}{3+4\lambda^2}(-f' + (\xi' - \omega_{x'})) \\ \frac{6}{3+4\lambda^2}(g' + (\eta' - \omega_{y'})) \\ 0 \end{pmatrix}_{z'=+b} \right]. \tag{18}$$

From Eq. (18), the torque $\mathbf{M}_c^c$, computed using the velocity gradients at the particle center of mass, and the torque $\mathbf{M}_c^m$, computed using the velocity gradients averaged along the particle length, can be obtained and the
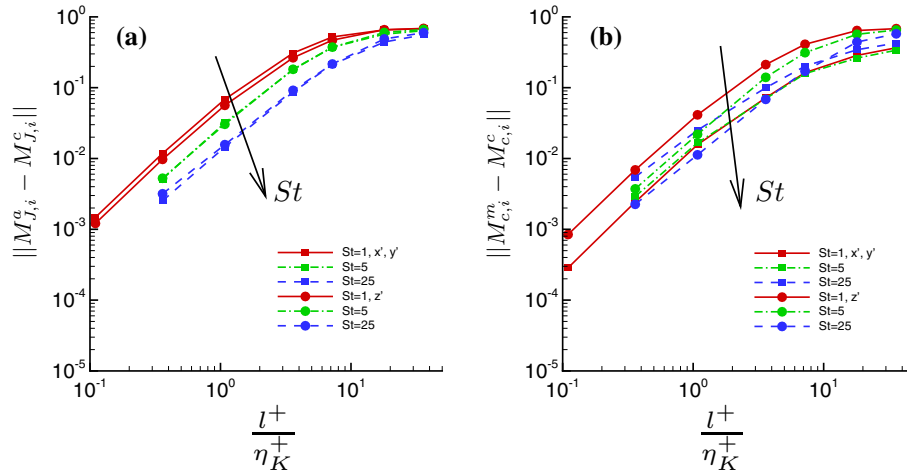
Fig. 5 Rms error (norm) for hydrodynamic torques at varying particle length, normalized by the reference Kolmogorov length scale $\eta_k^+ = 2$. Panels: **a** rms error for torques on a prolate ellipsoid; **b** rms error for torques on a cylinder

norm $||\mathbf{M}_c^m - \mathbf{M}_c^c||$ calculated. The behavior of the components of $||\mathbf{M}_J^a - \mathbf{M}_J^c||$ and $||\mathbf{M}_c^m - \mathbf{M}_c^c||$ at varying particle length and inertia is shown in Fig. 5: Specifically, the x'- and y'-components (which are identical) are represented by the filled squares, and the z'-component is represented by the filled circles. The norms increase with length reaching an asymptotic value for very long particles ($l^+/\eta_K^+ > 10$ in our simulations). The rms error can be as high as 60 % since these particles extend across regions of flow where the velocity gradients change significantly, thus violating the conditions for which the Jeffery formulation is valid (regardless of their orientation). As far as particle inertia is concerned, we observe that the rms error decreases as the Stokes number increases. Therefore, the results provided by the Jeffery formulation are more accurate for particles with higher inertia. This can be explained considering that particles exhibit preferential concentration and preferential orientation. In the present flow configuration, the highest degree of preferential concentration and wall accumulation is observed for the $St = 25$ particles, which are also those with the strongest tendency to align in the streamwise (wall-parallel) direction. A similar trend was observed by Mortensen et al. [24,25] and by [20] for the same flow configuration. When particles are preferentially aligned with the streamwise direction, the fluid velocity gradients measured along the particle are subject to smaller variations compared to other orientations. This is especially true in the near-wall region, where the predominant velocity gradient is the one associated with the mean shear, $\partial u/\partial z$: Because of preferential orientation, the $St = 25$ particles are more likely to sample a nearly constant value of $\partial u/\partial z$, which is exactly the condition required for Jeffery's theory to be valid. Comparing the z'-components of the torque at varying St (filled circles), we find that an increase in particle inertia results in lower values of the norm. In addition, Fig. 5 also shows that inertia has a weaker effects on the norm along directions perpendicular to the particle major axis (filled squares).

Results shown in Fig. 5 demonstrate clearly that the rms error exhibits a power-law behavior for particles with $l^+/\eta_K^+ \leq 8$, followed by a plateau for longer particles. The simulation data in these two regions of the plot, below and above $l^+/\eta_K^+ \simeq 8$, can be approximated by a fit of the form $\alpha(l^+/\eta_K^+)^\beta$. The coefficients α and β providing the best fit are given in Table 2, while the resulting trends are shown in Fig. 6. In this figure, only the results relative to the z'-component of the torques are shown for ease of discussion. The particle length at which the power-law fits intersect is denoted by l_0^+ and provides a threshold value for the range of validity of the tabulated values for α and β. The expression $\alpha(l^+/\eta_K^+)^\beta$ can be further modified to incorporate the Stokes number dependence of the rms error incurred in the calculation of the Jeffery torques. Based on Table 2, we suggest the following correlation for the global rms error:

$$||\mathbf{M}_J^a - \mathbf{M}_J^c|| \approx 0.041 St^{-0.34} \left(\frac{l^+}{\eta_K^+} \right)^{1.44} \qquad \text{for} \qquad \frac{l^+}{\eta_K^+} < 8. \qquad (19)$$

This correlation may be useful to estimate a priori the expected error associated with Lagrangian tracking once the physical and geometrical parameters of the particle are known. Note that, according to Eq. (19), an rms

Table 2 Power-law fitting of the rms error quantified the $||\mathbf{M}_c^m - \mathbf{M}_c^c||$ norm

St	$l^+ < l_0^+$		$l^+ > l_0^+$		l_0^+/η_K^+
	α	β	α	β	
Wall-normal component (z')					
1	0.03738	1.4335	0.5506	0.0619	7.1
5	0.02502	1.4404	0.3572	0.1619	8.0
25	0.01216	1.4844	0.1650	0.3405	9.8
Streamwise (x') and spanwise (y') components					
1	0.04429	1.4127	0.5571	0.0562	6.5
5	0.02503	1.4403	0.3567	0.1623	8.0
25	0.01216	1.4842	0.1650	0.3407	9.8

Simulation data are fitted by a law of the form $\alpha(l^+/\eta_K^+)^\beta$. Values of the fitting coefficients α and β are given considering two different ranges: one for ellipsoidal particles with $l^+/\eta_K^+ < 8$ (for which the rms error increases significantly with length) and one for ellipsoidal particles with $l^+/\eta_K^+ > 8$, for which the error tends toward an asymptotic value. The dimensionless length at which the prediction of the two fits is the same is given by l_0^+
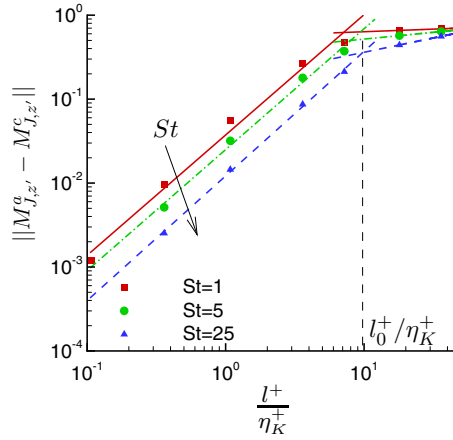
Fig. 6 Power-law fitting of the wall-normal component of Jeffery torques, corresponding to the coefficients in Table 2

error of about 4% should be expected for the Jeffery torques at $St = 1$ and $l^+/\eta_K^+ \simeq 1$, this error being much smaller at higher Stokes numbers.

To conclude our analysis, we examine the behavior of the rms error along the wall-normal coordinate. To this aim, we divided the channel into equally spaced, wall-parallel bins and averaged the torque components over all particles within each bin. The values so obtained were then averaged in time. The results are shown in Fig. 7. We observe that the rms error does not depend much on wall distance in the case of particles much longer than the Kolmogorov length scale. For shorter particles, we observe a smaller rms error for particles located in the central region of the channel (especially for those with low inertia in the top panels of Fig. 7) and for high-inertia particles in the near-wall region (bottom panels of Fig. 7). When moving close to the wall, long-enough particles are preferentially aligned in a plane parallel to the wall and do not experience the largest velocity gradients, which occur in the wall-normal direction: Accordingly, we observe a decrease of the rms error. On the other hand, low-inertia particles exhibit a low rms error in the center of the channel, where no preferential alignment is attained [20].

5 Conclusions

In this paper, we provide a statistical assessment of the application limits of the Jeffery formulation for hydrodynamic torques. The assessment is based on accurate DNS-based Eulerian–Lagrangian datasets for the reference case of prolate ellipsoidal particles and rod-like particles in turbulent channel flow. These elongated particles are typically used to model the behavior of rigid fiber suspensions in fluid flows. When their length is larger than the Kolmogorov length scale of turbulence, the flow field around the particles undergoes significant
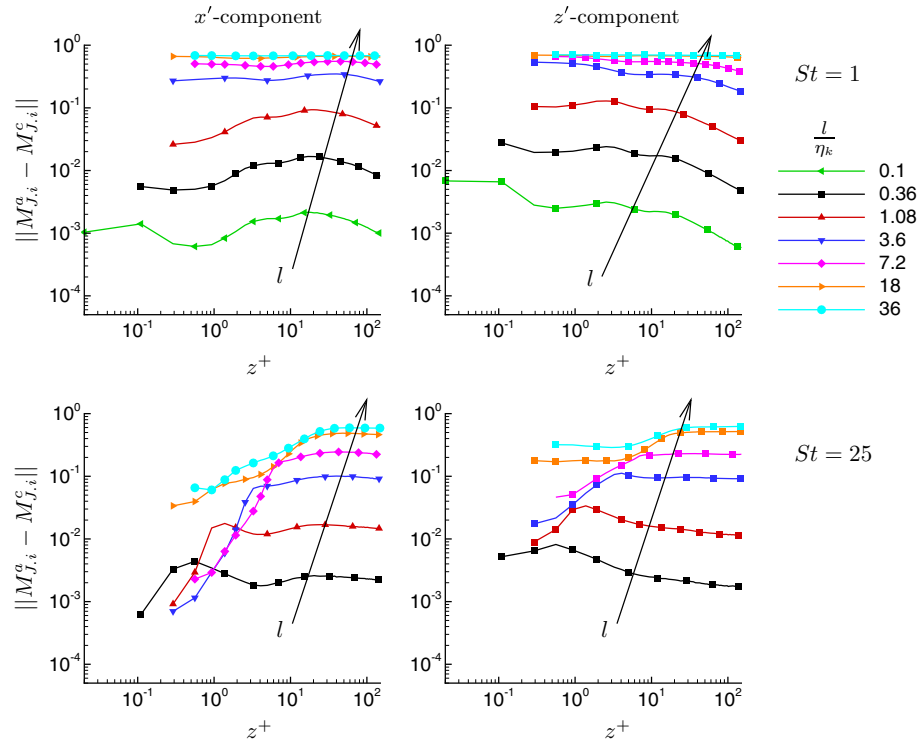
Fig. 7 Rms error (norm) for hydrodynamic torques on a prolate ellipsoidal particles as a function of the wall-normal coordinate. Top (resp. bottom) panels refer to the $St = 1$ (resp. $St = 25$) particles. Left-hand (resp. right-hand) panels refer to the rms error associated with the calculation of the streamwise (resp. wall-normal) component Jeffery torque component

spatial variations and cannot be approximated by extrapolation from the values attained by the fluid velocity at the center of mass of the particles. In turn, calculation of the torques based only on the velocity gradients at the center of mass becomes inaccurate. We have quantified such inaccuracy for particles with different size and different inertia. Our results show that the rms error associated with the use of the Jeffery formulation increases exponentially with particle length. However, the error is still tolerable (a few percents) for lengths of the order of the Kolmogorov scale and is found to decrease at increasing particle inertia. This suggests that Jeffery torques can grant acceptable accuracy when used to study the rotational dynamics of elongated particles characterized by nonzero values of the particle Reynolds number. From a practical point of view, it may be concluded that Jeffery-based Lagrangian tracking may be safely applied to environmental problems such as plankton dynamics in aquatic turbulence, since the size of planktonic organisms may vary from scales smaller than the Kolmogorov length of oceanic turbulence to scales lying within the inertial subrange of turbulence [7]. We expect the approach to be also applicable to problems in which particle dynamics is dominated by the larger and most energetic flow scales. In such a situation, large-eddy simulation (LES) of turbulence can be performed: In LES, only eddies of size larger than a given cut-off length scale ξ are computed, whereas eddies of size smaller than ξ are modeled. Typically, the condition $\xi > \eta_K$ holds, meaning that ξ is the smallest resolved length scale and that velocity gradients are smoothed out by filtering. This implies that the stringent point-particle DNS requirement $l << \eta_K$ relaxes to $l << \xi$, a condition that can be satisfied also by particles bigger than the Kolmogorov scale [3,23].

We also show that the magnitude of the error is affected by particle orientation only for particles smaller than the Kolmogorov scale: In this case, the error is much smaller for particles aligned in the streamwise direction (a condition that has a significant statistical occurrence in the near-wall region of bounded flows) compared to particles aligned in the wall-normal direction. The error for long particles is not very sensitive to their orientation. To complete the statistical characterization of the rms error, we also examined its behavior as a function of particle position relative to the wall. The error is found to depend weakly on particle distance from the wall for particles with low-inertia fibers, whereas high-inertia particles are characterized by a smaller error when they are located either very close to the wall or in the center of the channel.

References

1. Anczurowski, E., Mason, S.G.: Particle motions in sheared suspensions. XXIV. Rotation of rigid spheroids and cylinders. Trans. Soc. Rheol. **12**, 209–215 (1968)
2. Balachandar, S., Eaton, J.K.: Turbulent dispersed multiphase flows. Annu. Rev. Fluid Mech. **42**, 11–33 (2010)
3. Balachandar, S.: A scaling analysis for point-particle approaches to turbulent multiphase flows. Int. J. Multiph. Flow **35**, 801–810 (2009)
4. Brenner, H.: The Stokes resistance of an arbitrary particle. Chem. Eng. Sci. **18**, 1–25 (1963)
5. Brenner, H.: The Stokes resistance of an arbitrary particle—IV. Arbitrary fields of flow. Chem. Eng. Sci. **19**, 703–727 (1964)
6. Bretherton, F.P.: The motion of rigid particles in a shear flow at low Reynolds number. J. Fluid Mech. **14**, 284–304 (1962)
7. Byron, M., Einarsson, J., Gustavsson, K., Voth, G., Mehlig, B., Variano, E.: Shape-dependence of particle rotation in isotropic turbulence. Phys. Fluids **27**, 035101 (2015)
8. Capone, A., Romano, G.P., Soldati, A.: Experimental investigation on interactions among fluid and rod-like particles in a turbulent pipe jet by means of particle image velocimetry. Exp. Fluids **56**, 1 (2015)
9. Challabotla, N.R., Zhao, L., Andersson, H.I.: Orientation and rotation of inertial disk particles in wall turbulence. J. Fluid Mech. **766**, R2 (2015)
10. Chen, J., Jin, G., Zhang, J.: Large eddy simulation of orientation and rotation of ellipsoidal particles in isotropic turbulent flows. J. Turbul. **17**, 308–326 (2016)
11. Einarsson, J., Candelier, F., Lundell, F., Angilella, J.R., Mehlig, B.: Rotation of a spheroid in a simple shear at small Reynolds number. Phys. Fluids **27**, 063301 (2015)
12. Elghobashi, S.: On predicting particle-laden turbulent flows. Appl. Sci. Res. **52**, 309 (1994)
13. Gallily, I., Cohen, A.: On the orderly nature of the motion of nonspherical aerosol particles. J. Colloid Interface Sci. **68**, 338–356 (1979)
14. Gustavsson, K., Einarsson, J., Mehlig, B.: Tumbling of small axisymmetric particles in random and turbulent flows. Phys. Rev. Lett. **112**, 014501 (2014)
15. Hakansson, K.M.O., Kvick, M., Lundell, F., Prahl-Wittberg, L., Soderberg, L.D.: Measurement of width and intensity of particle streaks in turbulent flows. Exp. Fluids **54**, 1555 (2013)
16. Hinch, E.J., Leal, L.G.: Rotation of small non-axisymmetric particles in a simple shear flow. J. Fluid Mech. **92**, 591–608 (1979)
17. Hoseini, A.A., Lundell, F., Andersson, H.I.: Finite-length effects on dynamical behavior of rod-like particles in wall-bounded turbulent flow. Int. J. Multiph. Flow **76**, 13–21 (2015)
18. Jeffery, G.B.: The motion of ellipsoidal particles immersed in a viscous flow. Proc. R. Soc. A **102**, 161–179 (1922)
19. Kuerten, J.G.M.: Point-particle DNS and LES of particle-laden turbulent flow-a state-of-the-art review. Flow Turbul. Combust. **97**, 689–713 (2016)
20. Marchioli, C., Fantoni, M., Soldati, A.: Orientation, distribution and deposition of elongated, inertial fibers in turbulent channel flow. Phys. Fluids **49**, 033301 (2010)
21. Marchioli, C., Soldati, A.: Rotation statistics of fibers in wall shear turbulence. Acta Mech. **224**, 2311–2329 (2013)
22. Marchioli, C., Zhao, L., Andersson, H.I.: On the relative rotational motion between rigid fibers and fluid in turbulent channel flow. Phys. Fluids **28**, 013301 (2016)
23. Marchioli, C.: Large-eddy simulation of turbulent dispersed flows: a review of modelling approaches. Acta Mech. **228**, 738–768 (2017)
24. Mortensen, P.H., Andersson, H.I., Gillissen, J.J.J., Boersma, B.J.: Dynamics of prolate ellipsoidal particles in a turbulent channel flow. Phys. Fluids **20**, 093302 (2008a)
25. Mortensen, P.H., Andersson, H.I., Gillissen, J.J.J., Boersma, B.J.: On the orientation of ellipsoidal particles in a turbulent shear flow. Int. J. Multiph. Flow **34**, 678–683 (2008b)
26. Ni, R., Ouellette, N.T., Voth, G.A.: Alignment of vorticity and rods with Lagrangian fluid stretching in turbulence. J. Fluid Mech. **743**, R3 (2014)
27. Ni, R., Kramel, S., Ouellette, N.T., Voth, G.A.: Measurements of the coupling between the tumbling of rods and the velocity gradient tensor in turbulence. J. Fluid Mech. **766**, 202–225 (2015)
28. Njobuenwu, D.O., Fairweather, M.: Dynamics of single, non-spherical ellipsoidal particles in a turbulent channel flow. Chem. Eng. Sci. **123**, 265–82 (2015)
29. Parsa, S., Voth, G.A.: Inertial range scaling in rotations of long rods in turbulence. Phys. Rev. Lett. **112**, 024501 (2014)
30. Parsa, S., Guasto, J.S., Kishore, M., Ouellette, N.T., Gollub, J.P., Voth, G.A.: Rotation and alignment of rods in two-dimensional chaotic flow. Phys. Fluids **23**, 043302 (2011)
31. Parsa, S., Calzavarini, E., Toschi, F., Voth, G.A.: Rotation rate of rods in turbulent fluid flow. Phys. Rev. Lett. **109**, 134501 (2012)
32. Picciotto, M., Marchioli, C., Soldati, A.: Characterization of near-wall accumulation regions for inertial particles in turbulent boundary layers. Phys. Fluids **17**, 098101 (2005)
33. Pumir, A., Wilkinson, M.: Orientation statistics of small particles in turbulence. New J. Phys. **13**, 093030 (2011)
34. Ravnik, J., Hriberšek, M.: High gradient magnetic particle separation in viscous flows by 3D BEM. Comput. Mech. **51**, 465–474 (2013)
35. Rosen, T., Einarsson, J., Nordmark, A., Aidun, C.K., Lundell, F., Mehlig, B.: Numerical analysis of the angular motion of a neutrally buoyant spheroid in shear flow at small Reynolds numbers. Phys. Rev. E **92**, 063 (2015)
36. Sabban, L., van Hout, R.: Measurements of pollen grain dispersal in still air and stationary, near homogeneous, isotropic turbulence. J. Aerosol Sci. **42**, 867–882 (2011)
37. Shapiro, M., Goldenberg, M.: Deposition of glass fiber particles from turbulent air flow in a pipe. J. Aerosol Sci. **24**, 65–87 (1993)
38. Shin, M., Koch, D.L.: Rotational and translational dispersion of fibers in isotropic turbulent flows. J. Fluid Mech. **540**, 143–173 (2005)

39. Subramanian, G., Koch, D.L.: Inertial effects on the orientation of nearly spherical particles in simple shear flow. J. Fluid Mech. **557**, 257–296 (2006)
40. Taylor, G.I.: The motion of ellipsoidal particles in a viscous fluid. Proc. R. Soc. A **103**, 58–61 (1923)
41. Trevelyan, B.J., Mason, S.G.: Particle motions in sheared suspensions. I. Rotations. J. Colloid Sci. **6**, 354–367 (1951)
42. van Hout, R., Sabban, L., Cohen, A.: The use of high-speed PIV and holographic cinematography in the study of fiber suspension flows. Acta Mech. **224**, 2263–2280 (2013)
43. Voth, G., Soldati, A.: Anisotropic particles in turbulence. Annu. Rev. Fluid Mech. **49**, 249–276 (2017)
44. Zhang, H., Ahmadi, G., Fan, F.G., McLaughlin, J.B.: Ellipsoidal particles transport and deposition in turbulent channel flows. Int. J. Multiph. Flow **27**, 971–1009 (2001)
45. Zhao, L., Andersson, H.I.: Why spheroids orient preferentially in near-wall turbulence. J. Fluid Mech. **807**, 221–234 (2016)
46. Zhao, L., Marchioli, C., Andersson, H.I.: Slip velocity of rigid fibers in turbulent channel flow. Phys. Fluids **26**, 063302 (2014)
47. Zhao, F., van Wachem, B.: Direct numerical simulation of ellipsoidal particles in turbulent channel flow. Acta Mech. **224**, 2331–2358 (2013)
48. Zhao, F., George, W.K., van Wachem, B.G.M.: Four-way coupled simulations of small particles in turbulent channel flow: the effects of particle shape and Stokes number. Phys. Fluids **27**, 083301 (2015)